ACS OMEGA

http://pubs.acs.org/journal/acsodf

Article

Model Development for Nanosecond Laser-Induced Damage Caused by Manufacturing-Induced Defects on Potassium Dihydrogen Phosphate Crystals

Hao Yang,[§] Jian Cheng,*[,§] Zhichao Liu, Qi Liu, Linjie Zhao, Chao Tan, Jian Wang, and Mingjun Chen*

Cite This: *ACS Omega* 2020, 5, 19884−19895

Read Online

ACCESS | Metrics & More | Article Recommendations

ABSTRACT: Nanosecond laser-induced damage on (potassium dihydrogen phosphate) KDP crystals is a complex process, which involves coupled actions of multi-physics fields. However, the mechanisms governing the laser damage behaviors have not been fully understood and there have been no available models to accurately describe this complex process. In this work, based on the theories of electromagnetic, thermodynamic, and hydrodynamic fields, a coupled multi-physics model is developed to describe the transient behavior of laser-supported energy deposition and diffusion accompanied by the surface defect (e.g., surface cracks)-initiated laser damage process. It is found that the light intensification caused by the defects near the crystal surface plays a significant role in triggering the laser-induced damage, and a large amount of energy is quickly deposited via the light intensity-activated nonlinear excitation. Using the developed model, the maximum temperature of the crystal material irradiated by a 3 ns pulse laser is calculated, which agrees well with previously reported experimental results. Furthermore, the modeling results suggest that physical processes such as material melting, boiling, and flowing have effects on the evolution of the laser damage process. In addition, the experimentally measured morphology of laser damage sites exhibits damage features of boiling cores, molten regions, and fracture zones, which are direct evidence of bowl-shaped high-temperature expansion predicted by the model. These results well validate that the proposed coupled multi-physics model is competent to describe the dynamic behaviors of laser damage, which can serve as a powerful tool to understand the general mechanisms of laser interactions with KDP optical crystals in the presence of different defects.

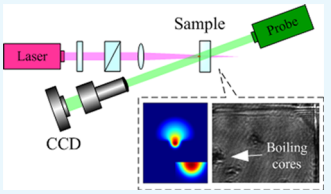

1. INTRODUCTION

Potassium dihydrogen phosphate (KDP) has been widely used in high-power laser systems for inertial confinement fusion (ICF) drivers such as National Ignition Facility (NIF) in the US, Laser MegaJoule in France, and Shenguang Laser Facility in China.[1−4] Currently, the low laser-induced damage threshold (LIDT) of KDP crystals has been the main factor, limiting the enhancement of the output laser flux of ICF drivers. Understanding the underlying mechanisms of laser-induced damage (LID) has significant practical applications in the fields from optical manufacturing to ignition engineering.[3,5,6]

The mechanism of LID for KDP crystals is complex, which has rapidly become a hot research area in recent decades.[7−10] With regard to the LID of transparent dielectric optical elements, the electron avalanche breakdown model has been proposed to explain the damage phenomenon.[11,12] Setting a critical limit of free electron density in the local area as the initiation of LID, the model successfully revealed the regime of the LID initiation process inside defect-free materials. In addition, theoretical damage models based on heat absorption and external impurities have been also reported.[13] The model explained the origin of LID from the perspective of impurities inside the boules and successfully predicted the damage initiation location, which is consistent with the experimentally observed random distribution of absorptive particles.

However, the underlying mechanisms of LID in KDP crystals have not been fully understood, especially for the surface damage induced by the mechanical defects. In the early days of KDP development, mainly the inclusions were discussed as a major obstacle in the advancement of the bulk LIDTs. Due to the improvement of the crystal growth technology and the advancement of the conditioning process at present,[14] the issues of bulk damage have been greatly alleviated and the bulk damage thresholds can reach the LIDTs of the surface damage. Nevertheless, it is found that surface structures such as pits, scratches, cracks, etc., are prone to induce laser damage in KDP crystals.[15−17] Because of the poor physical properties of KDP materials, like soft and brittle characteristics, temperature sensitivity, high water deliquescence, etc., it is inevitable to generate defects on the surface of

Received: June 18, 2020
Accepted: July 15, 2020
Published: July 29, 2020

https://dx.doi.org/10.1021/acsomega.0c02950
ACS Omega 2020, 5, 19884−19895

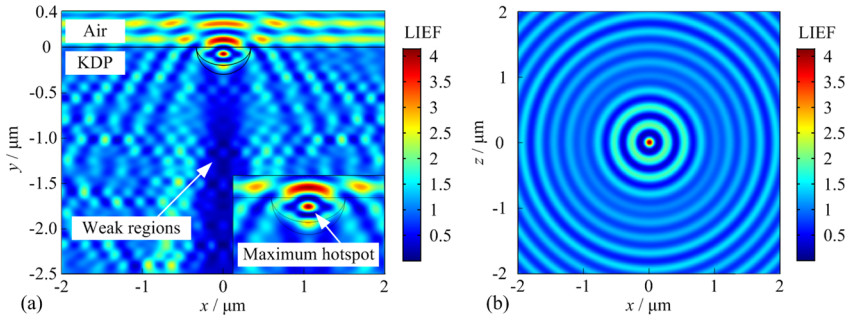

Figure 1. Distribution of light intensification by the lateral crack with the parameters of width w = 600 nm, total depth d_t = 300 nm, and gap depth d_g = 100 nm. (a) Distribution on the *xoy* profile of the KDP crystal. The inset represents the maximum light intensification of the electromagnetic field simulation. (b) Distribution on the *xoz* profile sectioning along the maximum hotspot.

the crystal during single-point diamond turning (SPDT) processes.[18,19] Nowadays, in the course of the development of KDP crystals with excellent quality and power-handling capability, the problem of laser-induced damage has shifted from the bulk to the surface. Based on the theory of electromagnetic field, the effect of structure parameters of crack defects on the light field enhancement was investigated.[15] The results showed that lateral cracks on the front surfaces and conical cracks on both front and rear surfaces can produce light intensification as high as hundreds of times, which is sufficient to launch avalanche ionization and reduces the laser damage resistance of KDP crystals. The model well simulated the influence of surface defects on the light energy transmission at the initial stage of the laser pulse. However, it is not able to obtain the energy evolution after the modulation of the light field and the subsequent behaviors of the damage processes. Therefore, a coupled model is needed to simulate the LID processes spatially and temporally with various physics laws.

Using the electromagnetic field, thermodynamics, and hydrodynamics methods, we first solve the light field distribution of a typical lateral crack on the front surface of KDP crystals and then calculate the temperature distribution during and after the laser duration. The modeling results show the effects of physical processes such as material melting, boiling, and flowing on the evolution of the laser damage process. Finally, through the artificial preparation of cracks and laser-induced damage tests on the crystal surface, the damage morphologies with boiling cores, molten regions, and fracture zones were observed, which further confirms the effectiveness of the proposed model. This work provides several methods for the research of LID. The results have offered further insights into understanding the initiation and evolution processes of LID. This work could play an important role in exploring the LID mechanisms caused by surface defects on KDP crystals. In addition, the results related to the evolution of defects on the KDP surface under intense laser irradiation can also provide technical support for optimizing the mechanical processes to achieve high-quality optical surfaces with high laser damage resistance.

2. RESULTS AND DISCUSSIONS

2.1. Light Intensity Distribution Calculated by the Electromagnetic Field Model. Light intensity enhancement factor (LIEF) is introduced to quantitatively characterize the localized light intensification caused by surface cracks.[15,20] Figure 1 depicts the light intensification profile modulated by the lateral crack on the front KDP surfaces. The lateral crack is 600 nm wide and 300 nm deep totally with a narrow gap of 100 nm. Due to the unique geometry of the lateral crack, significant diffraction occurs during laser propagation. The laser is incident along the front surface of the crystal. When it propagates through the lateral crack, the reflection and refraction of light will occur at the crack boundary. Once reflected light, the refracted light, and other incident light intersect at a certain point, the light intensity may increase sharply due to the phase addition of the light wave. In the center of the lateral crack, there is a distinct light intensity hotspot due to the effect similar to the lens focusing.[15] Compared with the intensity of the uniform distribution of light field inside the perfect crystal, the local light intensity can be enhanced up to more than 4 times. However, it is believed that damage is likely to occur when the LIEF is greater than 3.[21] Thus, this is unbearable for optical components such as KDP crystals. On the other hand, due to the lower mechanical properties, heat sensitivity, and enhanced absorption rate of the defects,[22] the damage at the position of the hotspot near the defects is more likely to occur. For other regions inside the KDP crystal, the light intensity distribution also exhibits obvious fluctuations. Distinct diffraction patterns as shown in Figure 1b can be observed on the *xoz* profile at $y = -74$ nm, which is the location of the light intensity hotspot. Especially, in the back side of the lateral crack on the *xoy* profile as shown in Figure 1a, the weak region is formed by a standing wave. Even some dark field can be seen on the simulated cross section. Uneven energy distribution inside the KDP crystal will have serious impacts on the damage. However, how light intensification affects the subsequent damage processes, the electromagnetic field model does not give an accurate explanation. Therefore, in the thermodynamics and hydrodynamics simulations, we use the local energy hotspot calculated by the electromagnetic field model as an input condition and simulate the influence of the lateral crack on the energy absorption, thermal field distribution, and other damage processes during laser irradiation. In general, the hotspot generated by the lens effect of the lateral crack will greatly reduce the laser damage resistance of the KDP crystal and play a dominant role in the damage initiation throughout the damage processes.

2.2. Temperature Distribution Simulated by the CET Model. Coupled with the results of the electromagnetic field model, as well as the Beer–Lambert law and Fourier heat conduction theory, the local temperature in the damage region is solved under a pulsed laser (3 ω, 5 GW/cm^2, and 3 ns). Since the energy integral of the rising edge of the laser pulse is less than the ideal state, the initial time of the solution is

https://dx.doi.org/10.1021/acsomega.0c02950
ACS Omega 2020, 5, 19884−19895

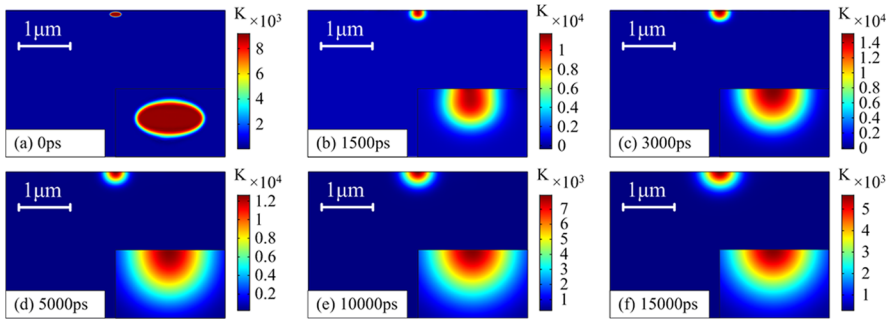

Figure 2. 2D simulations of temperature distribution inside the KDP crystal by the CET model at different times during and after laser irradiation. (a–f) are at t = 0, 1500, 3000, 5000, 10,000, and 15,000 ps, respectively.

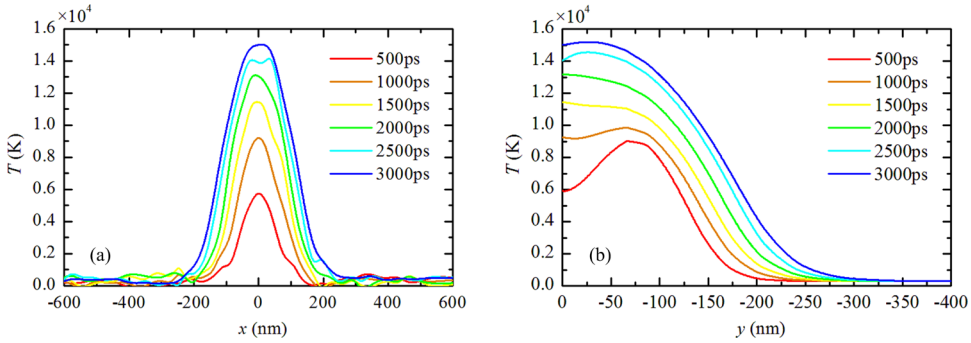

Figure 3. Temperature changes of KDP crystals simulated by the CET model at different times during laser irradiation. (a, b) 1D curves distributed along the x axis on the front surface and the y axis on the center line of the model during laser irradiation, respectively.

postponed with several picoseconds. Two-dimensional (2D) simulations of temperature distribution on the profile of the xoy profile at z = 0 inside the KDP crystal by the CET model at different times during and after the laser irradiation are shown in Figure 2, where (a–f) are at 0, 1500, 3000, 5000, 10,000, and 15,000 ps, respectively. Comparing the 2D temperature simulations near the surface defects during and after laser irradiation, the main behavior is an interaction between the crystal material and the strong laser, which would cause absorption and transport of laser energy inside the crystal. The high-temperature region gradually expands outward. During the period of 0–3000 ps (the laser duration), the region changes from an initial ellipse to a long strip in the reverse direction of laser propagation and finally appears to be a semicircle-like bowl shape. It indicates that the initial thermal distribution under laser action is related to the distribution and size of the light intensity hotspot induced by the defects. The subsequent high-temperature region changes to a bowl shape, which is dependent on the laser pulse parameters. Due to the correlation between the heat absorption coefficient of the material and the temperature, it is considered that a bowl-shaped heat absorbing region is formed in the late stage of the laser pulse. When the laser energy disappears, the internal temperature of the crystal begins to decrease, but the high-temperature region still expands as time goes by. The distribution of the high-temperature region differs from that during the laser action. At this time, the morphology of the high-temperature zone is almost similar, as shown in Figure 2d–f. However, its relative size is increasing from 426 to 707 nm. Moreover, according to the 2D simulations, the expansion rate of the high-temperature region remains almost constant (~28 m/s), which indirectly reflects that the energy distribution inside the crystal at the later time is mainly related to the laser parameters.

Figure 3a,b shows the 1D curves distributed along the x axis on the front surface and the y axis on the center line of the model during laser irradiation, respectively. The distance between every two neighbors of temperature curves from 500 to 3000 ps is continuously reduced, indicating that there is an initial moment of strong nonlinearity induced by surface defects under laser irradiation, which leads to a huge amount of local energy deposition and instantaneous temperature increase. During subsequent laser irradiation, the temperature of the crystal gradually increases as a whole but the rising rate decreases. It is deduced that it is mainly related to the energy diffusion limit between crystal lattices. The maximum temperature of the KDP surface is located directly above the hotspot of the defect-induced light intensity. The surface temperature is almost the highest except for the surface temperature at 500 ps, which is lower than the temperature of the body. From the results, it can be considered that the position on the crystal surface directly above the hotspot is the weakest region of laser-induced damage. It is very likely to be transformed into a thermal damage pit during the damage evolution processes. As for the expansion of the heat absorption front of the crystal, the lateral and radial heat absorption fronts at 3000 ps are located at x = ±250 nm and y = 300 nm, respectively. Although the heat diffuses rapidly in the radial direction from the surface, it is mainly related to the position of the initial hotspot along the radial depth of the crystal. In terms of the relative positional change of the heat absorption fronts, the lateral and radial relative expansion displacements from 150 to 3000 ps are both 100 nm, which suggests that the expansion speeds are similar. By performing a time-resolved investigation of the emission that is produced by the heated damage material, Carr et al.[23]

https://dx.doi.org/10.1021/acsomega.0c02950
ACS Omega 2020, 5, 19884–19895

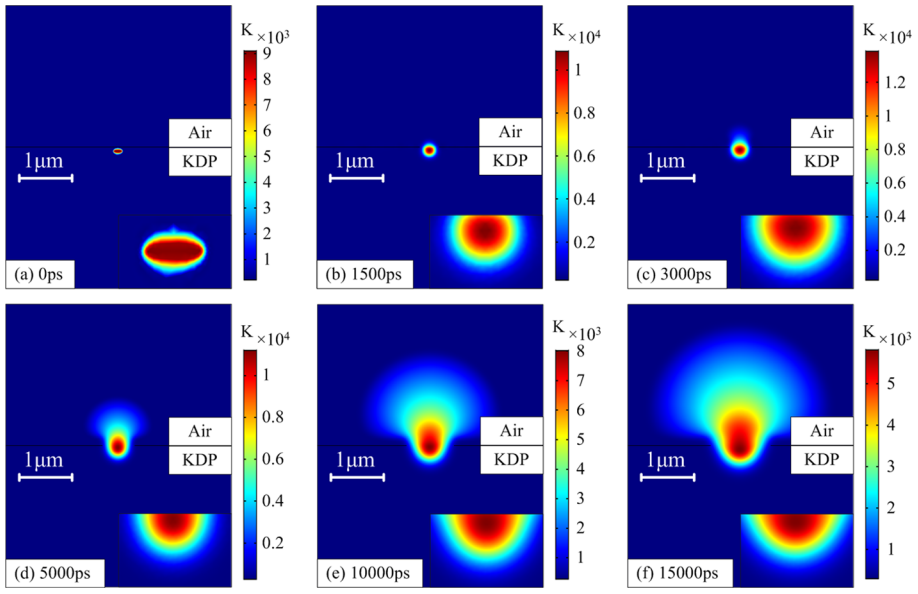

Figure 4. 2D simulations of temperature distribution inside the KDP crystal by the CETH model at different times during and after laser irradiation. (a–f) are at t = 0, 1500, 3000, 5000, 10,000, and 15,000 ps, respectively.

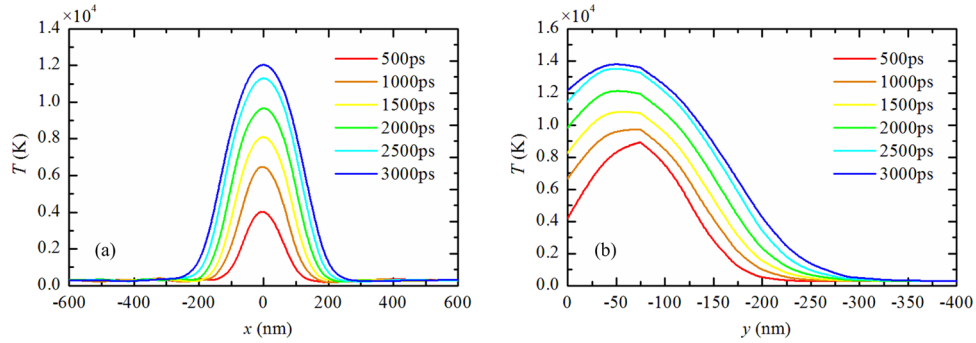

Figure 5. Temperature changes of KDP crystals simulated by the CETH model at different times during laser irradiation. (a, b) 1D curves distributed along the x axis on the front surface and the y axis on the center line of the model during laser irradiation, respectively.

measured the local temperature of the crystal material during strong laser irradiation based on the blackbody principle. When the crystal material is exposed with strong laser irradiation (~5 GW/cm^2, 355 nm), the results of damage dynamic experiments show that the local temperature of laser damage at 3 ns is 11,800 K. Compared with the simulations that the maximum surface temperature at the end time of 3 ns is 15,026 K, they are on the same temperature level with a difference of nearly 4000 K. This shows that the CET model makes sense to a certain extent. However, it also implies that factors such as melting, evaporation, and fluid flow play a critical role in the damage processes, which would greatly influence the calculation.

In a word, the CET model can roughly simulate the temperature change inside the crystal during and after irradiation of the strong laser, but the model needs further modification as well.

2.3. Temperature Distribution Simulated by the CETH Model. In order to optimize the temperature simulations of the CET model, the multi-physics CETH model combined with a series of physical laws such as material melting, boiling, and flowing is established based on Darcy's law, phase-field method, and Navier–Stokes equation. The simulated local temperature distributions on the profile of the xoy profile at z = 0 in the damage area are shown in Figure 4. Figure 4a–f shows the temperature distribution of the cross sections at different times calculated by the CETH model during and after the pulsed laser.

Compared with the simulations of the CET model, it can be seen that the 2D temperature distributions obtained by these two methods are similar at the initial time of t = 0 ps. However, as the time of laser irradiation increases, the high-temperature region obtained by the CETH model is close to spherical at t = 1500 ps. In addition, after the end time of the laser pulse (t > 3000 ps), the high-temperature region has always exhibited a bowl shape. The width–depth ratios of the high-temperature region at t = 5000, 10,000, and 15,000 ps are 1.81, 2.16, and 2.34, respectively. The values increase with time, which is quite different from the CET model. As for the overall temperature distribution inside the crystal, the diffusion speed is slightly higher than that in Section 2.2. This phenomenon may be due to the physical processes of material melting, evaporation, and flow. When the internal heat distribution of the material is not uniform, the fluid convection will play a considerable role in material energy exchange. In addition, it may be caused by the influence of the fluid boundary layer. Once the phase change interface produces a large speed difference, the influence of the fluid viscosity force near the wall surface cannot be ignored.

https://dx.doi.org/10.1021/acsomega.0c02950
ACS Omega 2020, 5, 19884–19895

The velocity of the boundary layer changes gradually, and the dissipation of kinetic energy will be expressed in the form of thermal energy. Therefore, a large temperature gradient is generated near the boundary layer, and the form of energy exchange is more diverse, which will eventually improve the energy diffusion efficiency of the damaged region.

Combined with the 1D simulations of temperature variation at different radial positions along the center line during pulse laser irradiation (see Figure 5b), the heat absorption center, which is the position with the highest temperature, is located below the front surface and gradually moves toward it. However, in Section 2.2, in addition to the initial state of the pulse laser, the heat absorption center is almost always on the front surface of the crystal. According to the previous report on laser damage of optical components, the thermally induced plasma appears below the front surface during the front surface damage and gradually grows in the opposite direction of laser propagation during laser irradiation.[24−26] Therefore, we can believe that the high-temperature center corresponds to the plasma observed during the damage transient processes, which will gradually move to the front surface with the laser action, and has a greater effect on heating the surrounding material. The energy of the laser pulse reduces rapidly at t = 3000 ps. At this time, the maximum temperature of the damaged area is 13,855 K, which is still slightly higher than the experimentally obtained temperature of 11,800 K.[23] However, the 1D temperature simulations at different moments on the front surface of the crystal during laser irradiation (see Figure 5a) indicate that the maximum temperature on the front surface is 12,172 K at t = 3000 ps, which is closer to the experimentally detected results. However, there are three questions at this stage. First, the specific location of the damage area (such as the crystal inside, the front surface, or the plasma in the air) in the experiments is unknown. Second, natural convection and radiation on the crystal surface, even the chemical changes such as dehydration and decomposing due to the high temperature in the damage processes, are ignored when building the multi-physics coupling model. Third, the plasma generated during laser irradiation will shield the KDP crystal, which will result in a decrease in the deposition energy inside the crystal. However, these three points will affect the final solution of the damage model more or less.[27] In addition, as can be seen from Figure 5a,b, the temperature differences at different times are smaller than those presented in Section 2.2, which also confirms that the models possess higher stability and accuracy to the reality when considering as comprehensive multiple physical factors as possible on the laser damage processes.

2.4. Comparison of Temperatures Calculated by the CET Model and CETH Model. Based on the results of the above models, we select the maximum temperatures of the crystal at different times during and after laser irradiation and draw the curves of temperature versus time, which are shown in Figure 6. The red line represents the temperature curve calculated by the CET model, and the blue line represents the temperature curve obtained by the CETH model. The laser is loaded by a flat-top pulsed laser with a wavelength of 355 nm, an intensity of 5 GW/cm^2, and a pulse width of 3 ns, as shown by the black curve. The maximum temperatures corresponding to the calculations of the two models are 15,026 and 13,855 K, respectively, with a difference of 1171 K. These values appear at the time of around 3000 ps. However, there is a little delay in the maximum temperature calculated by the CET model.

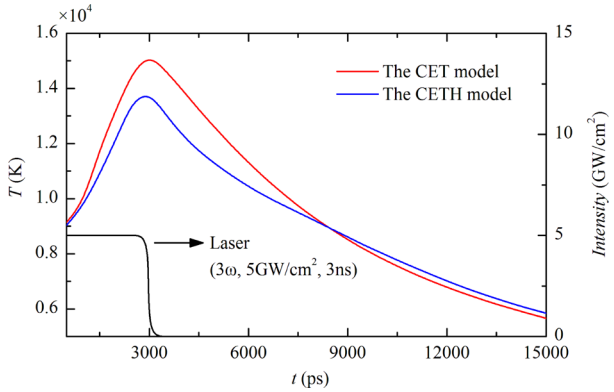

Figure 6. Comparison of the maximum temperature variations with respect to time calculated by the CET model and CETH model.

The temperature during laser irradiation calculated by the CET model is much higher than that calculated by the CETH model. The general understanding is that with the CETH model considering the cooling effect of the phase transition processes such as melting and gasification, the fluid flow would increase the thermal diffusion inside the crystal. After the end of laser pulse irradiation, the maximum temperatures of the crystal obtained by the two models start to reduce, but the temperature decrease calculated by the CET model is more obvious. The two curves meet at around 8000 ps. Before this time, the calculated temperature of the CET model is higher than that of the CETH model. After t = 8000 ps, the temperature calculated by the CETH model is slightly higher than that of the CET model. It means that the temperature-fall period corresponding to the results of the CETH model is more moderate. It is inferred that the external gaseous medium works. During pulse laser irradiation, the KDP crystal first interacts with the laser to deposit a huge amount of laser energy and the surrounding gas medium is passively heated. Since the gas part stores a large amount of energy, when the laser pulse stops, the external gaseous medium plays a key role in energy supply and heat insulation through energy exchange with the crystal. Compared with the experimentally detected temperature in the laser damage test,[23] the results of the CETH model agree with the real situation better. The results of damage dynamic experiments show that the local area of laser damage at 3 ns is 11,800 K. Although there are some errors between the simulations and the experiments, the temperature calculated by the CETH model is closer to the experimental data than that of the CET model. The physical processes such as material melting, boiling, and flowing during the damage processes have an inhibitory effect on the damage evolution for the cooling effect.

2.5. Results of Laser Damage Test. The laser damage occurred when the cracks around the indentation on the front KDP surface were irradiated by a laser pulse with a 355 nm wavelength and 20 J/cm^2 fluence. Figure 7 shows the transient behavior of the laser damage process at 0 ns delay (initial state) and 10 ns delay. At the initial time of laser irradiation, there is no damage site except the artificial surface defects. At time t = 10 ns, three circular black shadows appear in the original lateral crack area. The shape and appearance time of the shadow are consistent with the simulations of temperature distribution in Section 2.3. Thus, it is detected that the dark shadow is the boiling core of laser damage. As for the transient behaviors when the black shadow initially appears during the

https://dx.doi.org/10.1021/acsomega.0c02950
ACS Omega 2020, 5, 19884−19895

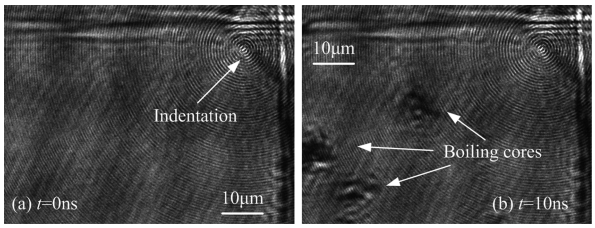

Figure 7. Transient behavior of the laser damage initiated by a 355 nm wavelength light and the cracks around the indentation on the front KDP surface at (a) 0 ns delay (initial state) and (b) 10 ns delay.

laser damage processes, we can infer that there would be shallow vignetting on the trigger point of the laser damage according to the predamage sites with the laser damage precursor being transformed.[28] When the lateral crack is irradiated with the strong laser beam, the hotspot of laser energy is generated by light intensification. A large amount of energy deposition near the surface defects would rapidly increase the local temperature. Then, the phase change of the KDP material like melting or boiling occurs. Due to a longer heating time of 10 ns delay, it is believed that the local temperature of the material is high enough to cause boiling. In addition, the dark shadows are caused by the effect of strong absorption by boiling matter for energy from the probe laser light. The high-temperature material forms a local blackbody region, causing the illumination light to not transmit completely. The dark shadows of boiling cores prove that the heat absorption coefficient of the damaged local area increases with the increase in temperature. The locations of the boiling cores are evidence that the laser damage is triggered by surface defects, which can lead to light intensification and energy deposition in the early period.

The SEM image of the damage morphology after single-shot irradiation of the 355 nm pulse laser is shown in Figure 8. In

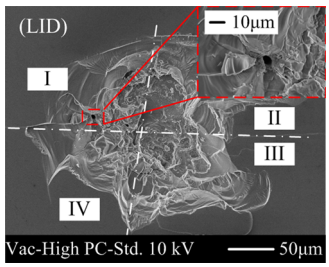

Figure 8. SEM image of the damage site initiated by a 355 nm wavelength light and the cracks around the indentation on the front KDP surface. The main image shows the whole area of the laser damage site. The inset is the enhanced microscopy image showing a small region of damage with the boiling core.

general, the damage size has a larger increase than that of the previous indentation pit. Traces of melting and fracture can also be clearly observed in the micrographs of the damage sites. In addition, the small boiling cores can be found in site I, which is similar to the bowl-shaped high-temperature area, as shown in the simulations. Obvious melting traces can be seen around the core, which is consistent with the damage morphology.[29−31] However, it is interesting that no similar core is found in the rest of the damage area. Only the deep and trim fracture can be seen at the damage boundary. Comparing with the microscopic images of the indentations with cracks, it can be found that the lateral crack in site II before laser irradiation is the neatest and clearest. Such crack clusters are most prone to generate strong energy accumulation. The mechanical strength of such cracks themselves is often the lowest. Therefore, we deduce that during the damage process in site II, the lateral crack leads to a large amount of energy deposition near the front surface of the crystal during pulse laser irradiation, and then a series of phenomena like melting, boiling, and flowing are generated. However, the local thermal stress produced by the uneven heat distribution causes a large stress concentration on the originally fragile boundary of lateral cracks, which makes the substrate material around the lateral cracks flew out as a whole part with the heated region and boiling core during the damage processes.[32] As a result, a deep and bordered damage pit is left. By carefully observing the damaged area, it can be found that there is a large piece of broken material at the bottom of site II, which can also provide evidence for this view. In addition, there is no lateral crack occurring in sites III and IV. In these areas, no source would initiate laser damage during laser duration. However, once the damage occurs, the weaker parts of the surrounding material are often destroyed and form a passive damage area due to thermal action. As for the laser damage probability, the damage probability of the perfect defect-free crystal surface is only 1/20 (5%) under single-shot irradiation with a fluence of 20 J/cm^2, which is much lower than the damage probability (90%) of artificial defects. This means that the existence of the cracks can greatly increase the damage probability. It also shows the evidence that the defects play a major role in initiating the laser damage on the KDP surface. In a word, the lateral crack in the experiment causes multiple damage sources to erupt at the same time during the damage processes. This provides a possibility to find obvious heat-affected regions in the final damage morphology. Combined with the above simulation analysis, the original damage process can be understood as a sharp light absorption point on the surface or subsurface of the KDP crystal induced by the defects. Then, the surrounding material interacts with the high-power laser. The temperature rise of the material is accompanied by melting, boiling, flowing, and even ejecting processes. In addition, the uneven distribution of the thermal field will cause a large thermal stress. Once there is a natural weak link inside the crystal, the material will be broken and a huge damage pit will be formed. However, the damage processes under the action of a nanosecond laser are inseparable from the thermal action in any case. The only difference is whether the phase changes of materials are caused by high temperatures or the material fracture is induced by a large thermal stress.

3. MODEL AND THEORY

As for simulating the processes of nanosecond laser damage, an electromagnetic field model or heat conduction model[33] is generally used. Sections 3.1−3.3 are the electromagnetic field model, the model coupling of electromagnetic field and thermodynamics (CET model for short), and the model coupling of electromagnetic field, thermodynamics, and hydrodynamics (CETH model for short), respectively, which are developed to describe the complex damage processes. In order to save the computing resources and improve the solving efficiency, we built a 2D model for laser damage simulation. Figure 9a is the schematic of the model for LID initiated by the lateral cracks on the front surface of the KDP crystal. Lateral cracks form below the surface in the plastic zone and propagate

https://dx.doi.org/10.1021/acsomega.0c02950
ACS Omega 2020, 5, 19884−19895

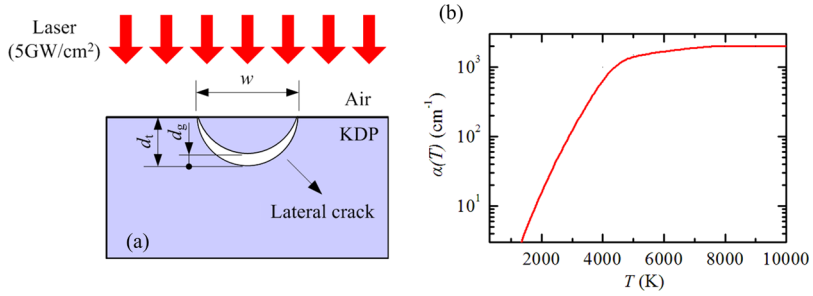

Figure 9. (a) Schematic of the model for LID initiated by the lateral cracks on the front surface of the KDP crystal. (b) Heat absorption coefficient $\alpha(T)$ dependent on the temperature T as the defined models.

parallel to the KDP surface. They are formed by residual elastic stresses caused by relaxation of the deformed material around the region of contact. These cracks extend upward to the surface and may join the radial cracks. When the lateral crack was completely propagated to the crystal surface, the boule material would be desquamated from the substrate. In order to study the effect of lateral cracks on laser damage, we choose unexfoliated lateral cracks as the research object in this work. Thus, the simplified crescent lateral crack shown in Figure 9a is built, where w is the crack width, and d_t and d_g are the total crack depth and the gap crack depth, respectively. The crack gap is considered to be an air medium. The incident laser light is a pulsed laser with a laser intensity of 5 GW/cm^2 at a wavelength of 355 nm. It should be noted that the anisotropy of material parameters has not been taken into consideration. Figure 9b is the heat absorption coefficient $\alpha(T)$, which is dependent on the temperature T and will be explained in detail in the following parts.

3.1. Electromagnetic Field Model. Due to the presence of machining defects on the crystal surface, the light field would be modulated during laser propagation. The distribution of light intensity can be obtained by solving Maxwell's equations of electromagnetic field.[20]

In this model, the overall width and height of the KDP domain are 4 and 2.5 μm, respectively. The plane wave with a 355 nm wavelength irradiates along the direction normal to the front KDP surface. Under the temperature of 20 °C and light wavelength of 355 nm, the relative dielectric constant ε_r is 1.54 (n^2_{KDP}), and two other electromagnetic parameters of relative magnetic permeability μ_r and electric conductivity σ are 1.0 and 0, respectively.

3.2. CET Model. The CET model mainly focuses on the physics of photon transport, laser energy deposition, and heat flow. So, as to investigate the influence of manufacturing-induced defects on the thermodynamics processes of the laser damage, we assume that the maximum hotspot of light intensity modulated by the surface defects would generate ionization at the initial moment and form a heat-absorbing sphere that is consistent with the hotspot in size. The presence of defects would affect the thermodynamic properties of the material, and there may be even free electrons or sub-band gap structures at the defect sites, which are easily excited under strong laser irradiation. The new free electrons absorb a lot of energy due to the high electromagnetic field.

The temperature variation inside the KDP crystal during the laser damage process is calculated by the heat transfer equation in eq 1. In addition, convection and radiation effects are included on the surface, but under the conditions of strong laser irradiation, they had little effect on energy deposition during the action of the laser pulse.[34]

$$\rho C\frac{\partial T}{\partial t} - \nabla\cdot(\kappa\nabla T) = Q = \alpha(T)I_{laser} \quad (1)$$

where ρ is the density of the KDP crystal, C is the heat capacity, κ is the thermal conductivity, and Q is the absorption energy of the crystal. Because the phase change is not taken into consideration, the effect of temperature on the material properties is neglected and these parameters are all defined with the solid-state parameters of KDP: ρ = 2338 kg·cm^{-3}, C = 2 J·K^{-1}·cm^{-3}, and κ = 1.9 W·m^{-1}·K^{-1}.[35] In order to compare with the measured local temperature of the experiments,[23] we adopted the laser intensity I_{laser} = 5 GW/cm^2, which propagates through the vertical direction toward the surface. $\alpha(T)$ is temperature-dependent heat absorption coefficient, and t is the time during laser pulse irradiation. T is the solution variable in the model.

During the interaction between the strong laser and the KDP crystal, the increase in temperature often leads to changes in the thermodynamic properties of the material. Therefore, the deposited energy from the laser pulse into the KDP crystal is solved by the Beer–Lambert law,[34,36] and the energy deposition process is dependent on the variation of the local absorption coefficient, which is simulated with respect to the temperature.

The heat absorption coefficient of the KDP crystal is dependent on the temperature, which is shown in Figure 9b. Fused silica and KDP are both transparent dielectric optics components with a wide band gap. The coefficient of KDP at 20 °C is 0.005 cm^{-1}, which almost has no effect on the laser energy transmission. Under strong laser irradiation, the local material temperature of the laser damage region rises sharply, which in turn would increase the subsequent laser energy deposition efficiency. The local temperature of the damage region on the KDP crystal can exceed 10,000 K at the end of laser duration. This indicates that the absorptivity $\alpha(T)$ of intrinsic defect-free KDP increases strongly with T. In addition, the material parameters would change greatly at the temperature of the phase change for KDP. Under those conditions, $\alpha(T$ = 2273 K) is sufficient to generate violent thermal absorption. When the temperature T increased by the absorption by surface defects is high enough, the material around would become absorbing. In addition, the absorption of the KDP material increases the temperature, which would increase $\alpha(T)$ in turn and eventually lead to destructively high temperatures.

Regarding the initial boundary conditions of the heat conduction model, it is very important to set the initial

https://dx.doi.org/10.1021/acsomega.0c02950
ACS Omega 2020, 5, 19884−19895

temperature of the hotspot. As previously noted, we assume the damage initiates at $t = 0$ ps. The initial temperature of the hotspot is ~9000 K inside the light intensity hotspot calculated by the multiphoton absorption model assisted by the sub-bandgap energy level structure near the defects.[27]

3.3. CETH Model. The damage process is complicated. When the temperature rises to a critical point, the processes of melting, boiling, flowing, etc., may influence the damage behavior. Therefore, in this model, the physical processes involved in different states like solid phase, liquid phase, and gas−liquid are individually described mathematically.

First of all, the whole model needs to meet the law of energy conservation and the governing equation is shown below:

$$\rho C\left[\frac{\partial T}{\partial t} + \nabla\cdot(\boldsymbol{v}T)\right] = \nabla\cdot(\kappa\nabla T) + I_{\text{laser}}\alpha(T) - \frac{\Delta L\dot{m}\delta(\varphi)}{M} \quad (2)$$

Here, the latent heat during the phase change ΔL is ~4048 J·mol. $\dot{m}$ is the phase change rate on the phase interface. δ is the Dirac delta function. φ is the solution variable of the phase-field equation, which will be illustrated in the following section. $\boldsymbol{v}$ is the velocity vector to describe the motion state of the damage area. In order to consider the effect of nonisothermal flow, the parameters related to particle velocity are added to eq 1. On the other hand, the phase change reaction due to the temperature rise in the material is a cooling process. Thus, the energy lost is added on the interface of phase change.

It is difficult to use one equation to describe the speed at each point in the solution domain of the hydrodynamic model. Thus, we use various methods for defining the momentum conservation in the solid−liquid phase, gas phase, and liquid−gas interfaces. The material in the solid and liquid phases is assumed to be incompressible. The velocity in these domains is described by the incompressible Navier−Stokes eq 3.[37]

$$\rho_{s,l}\left[\frac{\partial \boldsymbol{v}_{s,l}}{\partial t} + \boldsymbol{v}_{s,l}\cdot(\nabla\cdot\boldsymbol{v}_{s,l})\right] = \nabla\cdot[-p_{s,l}\boldsymbol{I} + \mu_l(\nabla\boldsymbol{v}_{s,l} + (\nabla\boldsymbol{v}_{s,l})^T)] + F_{\text{Darcy}} \quad (3)$$

with the unit matrix $\boldsymbol{I}$ and dynamic viscosity in the liquid phase μ_l. Considering the convection and diffusion in solid and liquid phases, the method of heat transfer in the porous medium interface is utilized. Based on the convection−diffusion theory, the average model of thermodynamic properties is used to describe the solid and fluid in the temperature equation. The solidification of the material would result in momentum loss. The lost momentum is calculated by the Darcy friction F_{Darcy} on the solid−liquid interfaces as shown below:

$$F_{\text{Darcy}} = K\boldsymbol{v}_{s,l} \quad (4)$$

$$K = -C\left(\frac{(1-f_l)^2}{f_l^3 + b}\right) \quad (5)$$

where K is the Carman−Kozeny coefficient in the porous medium model of the solid−liquid phase, which is the seepage coefficient as well.[38] The parameters of C and b are constants. In the calculations, C takes a larger value, and q takes a smaller value to ensure that the formula is meaningful.

A temperature-dependent function f_l is defined. When the temperature is much higher than the melting temperature of the crystal, its value is 1. When the temperature is much lower than the melting temperature of the crystal, its value is 0. When the local temperature is near the melting temperature, f_l takes a certain value between 0 and 1, depending on the accurate temperature, and at this time, the crystal is in a solid−liquid mixed state.

The Darcy friction is related to the value of f_l. The f_l of the pure liquid phase is 1, which corresponds to the Darcy friction of zero. When the f_l of the solid−liquid mixing zone ranges from 0 to 1, the value of K is determined by the unsteady convection and diffusion in the fluid dynamics equation. There is a very strong Darcy friction in the solid phase region with $f_l = 0$. It can be considered that the fluid in this region has a large dynamic viscosity coefficient, which makes the particle velocity approach to zero. The porous media model can describe the distribution of the velocity and the pressure in solid and liquid phases, as well as the solid−liquid transition process.

The material of the KDP crystal boils at temperatures above 3273 K.[39] The density of the material would change greatly with the variation of the temperature and pressure. The governing equation in the gas domain is the hydrodynamic equation in compressible form. Assuming that the KDP gaseous substance is an ideal gas, the density satisfies the ideal gas state equation. The boundary conditions of hydrodynamics at the interface between liquid and gas in this laser damage model are rather complicated because the interface velocity, liquid velocity, and gaseous velocity nearby are not necessarily equal. Once the phase change occurs and the liquid density is not equal to the gaseous density, the variation of the gaseous density will introduce an inward flow velocity normal to the interface. Then, there will be a velocity in the outward direction normal to the interface of the gas domain to make up for the speed difference. This leads to a discontinuity in the velocity field across the interface.

The continuity equations of hydrodynamics characterize the mass conservation in this system. However, some transformations are employed for governing equations on various calculation domains.

The solid−liquid phase is described by eq 6. The gas phase is built on eq 7.In addition, the continuity equation at the liquid−gas interface is modified with eq 8 to describe the phase change process.[40]

$$\nabla\cdot\boldsymbol{v}_{s,l} = 0 \quad (6)$$

$$\frac{\partial \rho_v}{\partial t} + \nabla\cdot(\rho_v\boldsymbol{v}_v) = 0 \quad (7)$$

$$\nabla\cdot\boldsymbol{v} = \dot{m}\delta(\varphi)\left(\frac{1}{\rho_v} - \frac{1}{\rho_l}\right) \quad (8)$$

In addition, the mass flux leaving the liquid−gas interface can be evaluated from the conductive heat flux shown in eq 9, which is obtained by neglecting the kinetic energy due to the viscous force.

$$\dot{m} = -\frac{\boldsymbol{n}\cdot M\kappa_v\nabla T}{\Delta L} \quad (9)$$

The equations above can describe the total transitions for the dynamics process of laser-induced damage. It is the fact that the arbitrary Lagrangian−Eulerian method is effective to solve these equations in principle, which is widely used in some previous work.[41] However, no topological changes can occur

https://dx.doi.org/10.1021/acsomega.0c02950
ACS Omega 2020, 5, 19884−19895

there. By making some suitable assumptions, the complex damage model can be perfectly solved on a fixed mesh with the phase-field method. Based on the Ginzburg−Landau and Cahn−Hilliard equations (two additional transport equations, one for the phase-field variable and the other for the mixing energy density), the advanced numerical method is particularly suitable for tracking interfaces with complex morphologies and motions. Also, the movement of the surface is determined by minimization of free energy. Thus, the algorithm is convenient and highly efficient. Combining with the phase-field method, the governing equation for simulating the liquid−gas interface during laser-induced damage processes can be represented as eq 10.[42] By tracing the liquid−gas interface, the gasification process can be simulated with the material detached from the element base, which is the most important expression of laser damage in the initial stage. It is also helpful for laser damage evolution analysis, such as liquid ejecting, by focusing on the unstable liquid−gas interface.

$$\frac{\partial \varphi}{\partial t} + \boldsymbol{v}\cdot\nabla\varphi - \dot{m}\delta(\varphi)\left(\frac{V_{f,l}}{\rho_l} + \frac{V_{f,g}}{\rho_g}\right) = \nabla\cdot\frac{\gamma\tau}{\varepsilon^2}\nabla\psi \quad (10)$$

where φ is a dimensionless phase-field variable, ranging from −1 to 1. The volume fractions of the liquid phase and the gaseous phase are $V_{f,l}$ and $V_{f,g}$, respectively, at the liquid−gas interface. The quantity γ is the mobility, τ is the mixing energy density, and ε is the capillary width that scales with the thickness of the interface. The mobility determines the timescale of the Cahn−Hilliard diffusion and must be large enough to retain a constant interfacial thickness but small enough so that the convective terms are not overly damped. In addition, the other two parameters of τ and ε are related to the surface tension coefficient.

4. EXPERIMENTAL SECTION

The effect of surface defects on LID of KDP crystals is experimentally investigated by performing LID tests and observing the morphology of damage sites. Because of the poor physical properties of KDP materials, like soft and brittle characteristics, temperature sensitivity, high water deliquescence, etc., it is inevitable to generate defects on the surface of the crystal during SPDT processes. The crack formation on KDP crystals can be also approximately equivalent to the process of repeated indentation of a mechanically loaded hard indenter (diamond tip) on the crystal surface during fly-cutting.[15] Through statistical analysis for the large amount fracture behavior of brittle materials, the microcracks on the surface or subsurface of the brittle materials (e.g., KDP crystals) are roughly divided into conical cracks, lateral cracks, and radial cracks.[43,44] As for the lateral cracks and the radial cracks, they are mainly generated by a sharp indenter, which is often the case for sharp diamond tools. Thus, the micro-indentation is an effective method to prepare defects of the radial and lateral cracks on brittle materials.[15,45] The radial and lateral cracks caused by the microindentation are slender planar cracks and crescentic cracks, respectively. They share the same shape with some of the defects caused by SPDT. In addition, the manufacturing-induced surface defects generally possess different dimensions (from nanometer to millimeter scale) in nature. The overall size of the surface cracks prepared by the microindentation method is dozens of micrometer, and the cracks in natural conditions of SPDT can reach the similar size. Moreover, due to the randomness of defect formation in SPDT processing, it is difficult to obtain multiple identical defects for damage experimental investigation. The micro-indentation method for surface defect preparation meets the challenges. Therefore, it is applied to produce defects on the KDP surfaces in this work. Figure 10 is the schematic diagram

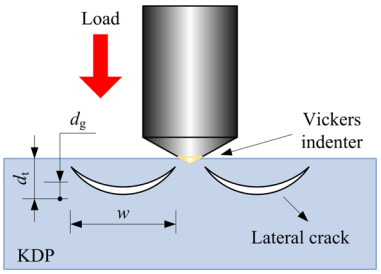

Figure 10. Schematic diagram of artificial lateral cracks prepared by a Vickers hardness tester.

of artificial lateral cracks prepared by a Vickers hardness indenter. A four-side pyramidal diamond tip on a standard Vickers indenter with a section angle of 136° is adopted to apply a load of 100 g (0.98 N) on the surface of the crystal. The maximum cross-sectional radius of the diamond is ∼500 μm. The nose radius of the indenter tip is ∼50 nm.

The indentations with peripheral cracks around on the crystal surface after loading are shown in Figure 11. BF

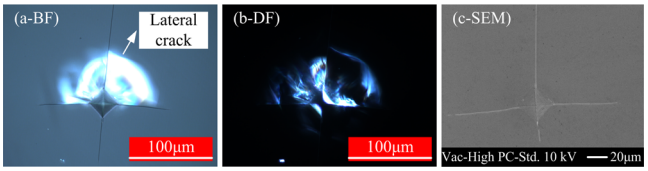

Figure 11. Indentations with peripheral cracks around on the crystal surface after loading. Here, bright-field optical micrograph, dark-field optical micrograph, and scanning electron micrograph are represented by SF, DF, and SEM, respectively.

represents the optical micrograph in the bright field of Vickers indentations and cracks around the KDP surface. DF represents the optical micrograph in the dark field, and SEM represents the scanning electron micrograph. Comparing the different micrographs of the indentation pit, there are four obvious radial cracks and lateral cracks around the indentation. The lateral cracks propagate narrowly to the KDP surface due to the connection of the KDP material in the lateral crack area, which meet the research requirements. Due to the anisotropy of the KDP crystal, the length of the radial cracks varies with the fracture direction. The upper radial crack is the longest, followed by the left and right cracks. The lower crack is the shortest. Furthermore, all of the lateral cracks almost take place above the indentation.

Figure 12 is the diagram of light paths for generating the laser-induced damage sites on KDP crystals and capturing the transient damage behavior near the surface defects. The pump laser light is emitted by a single longitudinal mode nanosecond laser, modulated and collimated, and then finally focused on the front surface of the KDP crystal. The energy regulator includes a $\lambda/2$ wave plate and a polarizer. The $\lambda/2$ wave plate can adjust the linear polarization direction of the output laser beam. When the linear polarized beam passes through a

https://dx.doi.org/10.1021/acsomega.0c02950
ACS Omega 2020, 5, 19884−19895

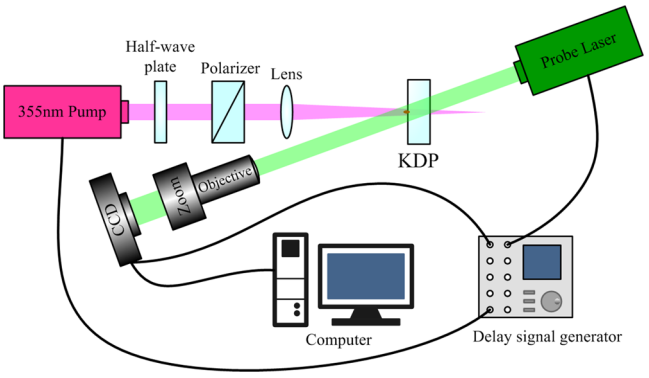

Figure 12. Diagram of light paths for generating the laser-induced damage sites on the KDP crystal and capturing the transient damage behavior near the surface defects.

polarizer placed at a fixed Brewster angle, only a specific component of the polarized beam can pass through. Thus, the combination of $\lambda/2$ wave plate and a polarizer can achieve the purpose of energy adjustment. A pulsed laser with a wavelength of 355 nm and pulse width of ∼8 ns (FWHM) is used to perform single-shot irradiation on each indentation pit and on the perfect defect-free KDP surface for comparison. The experimental laser duration is greater than that of the simulation. Thus, a laser fluence over 15 J/cm^2 is needed to irradiate the KDP crystal and cause laser damage. In addition, we found that the surface LIDT of the KDP crystal with the artificial defects is a little less than 20 J/cm^2. When the laser fluence is 20 J/cm^2, plasma is generated in the vicinity of the artificial defects under laser irradiation and the damage morphology is clearly visible. Therefore, the fluence is selected for the experiment. The output laser energy has a spatial distribution of the Gaussian profile on the front surface of the crystal with an effective spot diameter of 336 μm, which is larger enough to radiate the whole region of each defect. In addition, according to our previous work, the light intensity enhancement generated by the slender radial cracks is much lower than that generated by the lateral cracks. Therefore, we believe that the damage initiation is mainly caused by the lateral crack in this laser damage test.[15] However, it can be seen from the Figure 11 that even the lateral cracks in a certain location are not a single crack. They are a cluster formed by numerous cracks with various shapes and sizes. Thus, the small difference between the lateral cracks will inevitably affect the damage results. However, it also provides a good access to investigate the mechanism of LIDs initiated by the surface defects. As for the detection system for capturing the transient damage behavior, it consists of a probe laser and a microscopy imaging device.[46,47] The probe pulse with a 532 nm wavelength and ∼70 ps duration (FWHM) is used for strobe light illumination. The timing of the probe pulse in reference to the pump pulse is controlled by a delay signal generator. The resolution of relative time delay between pump and probe is ∼1 ns. In order to capture the process of transient transition for materials near the surface defects during laser damage, the microscope is positioned perpendicular to the surface of the sample on the air side. The focal plane of the microscope intersects at the sample's surface at the pump beam location.

5. CONCLUSIONS

Based on the theories of electromagnetic field, thermodynamics, and hydrodynamics, we simulated the distribution of light intensity and temperature evolution near a lateral crack on the KDP surface irradiated by a strong laser pulse with an intensity of 5 GW/cm^2. The calculations show that when the lateral cracks are located on the front surface of the crystal, a lens effect would occur. Also, the light field modulation will generate an intensified hotspot, which plays a triggering role in the process of laser-induced damage. Combining the CET model and the CETH model to solve the temperature distribution near the hotspot, the models can simulate the processes of sharp increase and slow decrease of temperature inside the crystal during and after the laser action. Compared with the experimentally detected temperature during laser damage processes in the previous report, the CETH model is more accurate and reliable because its calculations are closer to the experimental results than those calculated by the CET model. Thus, it is proved that physical processes such as material melting, boiling, and flowing during the damage processes have an inhibitory effect on the damage evolution due to the cooling effect. Owing to the existence of bowl-shaped high-temperature regions near the defects, the boiling cores and molten regions in the damaged areas are also probably to be generated, which has been well verified by the laser damage test and temperature detection experiments. In addition, a large amount of material fracture zone is experimentally observed in the damaged sites. The thermal stress accumulation and weak mechanical properties of the crystal with defects should be responsible for the fracture damage features. In general, the thermal effect induced by nanosecond laser irradiation plays a key role in the damage processes that the direct melting, evaporation, or indirect thermal stress-induced fracture greatly contribute to the final damage morphology. This work not only deepens our understanding in nanosecond laser-induced damage mechanisms for transparent dielectric optics components but also provides potential insights into how to improve their laser damage resistance.

AUTHOR INFORMATION

Corresponding Authors

Mingjun Chen − *State Key Laboratory of Robotics and System, Harbin Institute of Technology, Harbin 150001, China*; Email: chenmj@hit.edu.cn

Jian Cheng − *State Key Laboratory of Robotics and System, Harbin Institute of Technology, Harbin 150001, China*; Email: cheng.826@hit.edu.cn

Authors

Hao Yang − *State Key Laboratory of Robotics and System, Harbin Institute of Technology, Harbin 150001, China; Research Center of Laser Fusion, China Academy of Engineering Physics, Mianyang 621900, China*; orcid.org/0000-0003-3625-1517

Zhichao Liu − *Research Center of Laser Fusion, China Academy of Engineering Physics, Mianyang 621900, China*

Qi Liu − *State Key Laboratory of Robotics and System, Harbin Institute of Technology, Harbin 150001, China*

Linjie Zhao − *State Key Laboratory of Robotics and System, Harbin Institute of Technology, Harbin 150001, China*

Chao Tan − *State Key Laboratory of Robotics and System, Harbin Institute of Technology, Harbin 150001, China*

Jian Wang − *Research Center of Laser Fusion, China Academy of Engineering Physics, Mianyang 621900, China*

Complete contact information is available at:

https://dx.doi.org/10.1021/acsomega.0c02950
ACS Omega 2020, 5, 19884−19895

https://pubs.acs.org/10.1021/acsomega.0c02950

Author Contributions

§H.Y. and J.C. contributed equally to this work.

Notes

The authors declare no competing financial interest.

■ ACKNOWLEDGMENTS

This work was financially supported by the Science Challenge Project (no. TZ2016006-0503-01), by the National Natural Science Foundation of China (nos. 51775147 and 51705105), by the Young Elite Scientists Sponsorship Program by CAST (no. 2018QNRC001), by the China Postdoctoral Science Foundation (nos. 2017M621260 and 2018T110288), by the Heilongjiang Postdoctoral Fund (no. LBH-Z17090), and by the Self-Planned Task Foundation of State Key Laboratory of Robotics and System (HIT) of China (no. SKLRS201718A).

■ REFERENCES

(1) Moses, E. I.; Lindl, J. D.; Spaeth, M. L.; Patterson, R. W.; Sawicki, R. H.; Atherton, L. J.; Baisden, P. A.; Lagin, L. J.; Larson, D. W.; MacGowan, B. J.; Miller, G. H.; Rardin, D. C.; Roberts, V. S.; Van Wonterghem, B. M.; Wegner, P. J. Overview: Development of the National Ignition Facility and the Transition to a User Facility for the Ignition Campaign and High Energy Density Scientific Research. *Fusion Sci. Technol.* **2017**, *69*, 1−24.

(2) Hawley-Fedder, R. A.; Geraghty, P.; Locke, S. N.; McBurney, M. S.; Runkel, M. J.; Suratwala, T. I.; Thompson, S. L.; Wegner, P. J.; Whitman, P. K. NIF Pockels cell and frequency conversion crystals. In *Optical Engineering at the Lawrence Livermore National Laboratory II: The National Ignition Facility*; International Society for Optics and Photonics: 2004, *5341*, 121.

(3) Manes, K. R.; Spaeth, M. L.; Adams, J. J.; Bowers, M. W.; Bude, J. D.; Carr, C. W.; Conder, A. D.; Cross, D. A.; Demos, S. G.; Di Nicola, J. M. G.; Dixit, S. N.; Feigenbaum, E.; Finucane, R. G.; Guss, G. M.; Henesian, M. A.; Honig, J.; Kalantar, D. H.; Kegelmeyer, L. M.; Liao, Z. M.; MacGowan, B. J.; Matthews, M. J.; McCandless, K. P.; Mehta, N. C.; Miller, P. E.; Negres, R. A.; Norton, M. A.; Nostrand, M. C.; Orth, C. D.; Sacks, R. A.; Shaw, M. J.; Siegel, L. R.; Stolz, C. J.; Suratwala, T. I.; Trenholme, J. B.; Wegner, P. J.; Whitman, P. K.; Widmayer, C. C.; Yang, S. T. Damage Mechanisms Avoided or Managed for NIF Large Optics. *Fusion Sci. Technol.* **2017**, *69*, 146−249.

(4) Baisden, P. A.; Atherton, L. J.; Hawley, R. A.; Land, T. A.; Menapace, J. A.; Miller, P. E.; Runkel, M. J.; Spaeth, M. L.; Stolz, C. J.; Suratwala, T. I.; Wegner, P. J.; Wong, L. L. Large Optics for the National Ignition Facility. *Fusion Sci. Technol.* **2017**, *69*, 295−351.

(5) Norton, M. A.; Adams, J. J.; Carr, C. W.; Donohue, E. E.; Feit, M. D.; Hackel, R. P.; Hollingsworth, W. G.; Jarboe, J. A.; Matthews, M. J.; Rubenchik, A. M.; Spaeth, M. L. Growth of laser damage in fused silica: diameter to depth ratio. In *Laser-Induced Damage in Optical Materials*; International Society for Optics and Photonics: 2007, *6720*, 67200H.

(6) Van Wonterghem, B. M.; Brereton, S. J.; Burr, R. F.; Folta, P.; Hardy, D. L.; Jize, N. N.; Kohut, T. R.; Land, T. A.; Merritt, B. T. Operations on the National Ignition Facility. *Fusion Sci. Technol.* **2017**, *69*, 452−469.

(7) Lamaignère, L.; Chambonneau, M.; Diaz, R.; Courchinoux, R.; Donval, T. Laser damage resistance qualification of large optics for high power laser. In *High Power Lasers for Fusion Research III*; International Society for Optics and Photonics: 2015, *9345*, 934508.

(8) Carr, C. W.; Feit, M. D.; Johnson, M. A.; Rubenchik, A. M. Complex morphology of laser-induced bulk damage in $K_2H_{(2-x)}D_xPO_4$ crystals. *Appl. Phys. Lett.* **2006**, *89*, 131901.

(9) Negres, R. A.; Kucheyev, S. O.; DeMange, P.; Bostedt, C.; van Buuren, T.; Nelson, A. J.; Demos, S. G. Decomposition of KH_2PO_4 crystals during laser-induced breakdown. *Appl. Phys. Lett.* **2005**, *86*, 171107.

(10) Cheng, J.; Wang, J.; Peng, E.; Yang, H.; Chen, H.; Chen, M.; Tan, J. Combined modulation of incident laser light by multiple surface scratches and their effects on the laser damage properties of KH_2PO_4 crystal. *Opt. Express* **2020**, *28*, 8764.

(11) Bloembergen, N. Laser-induced electric breakdown in solids. *IEEE J. Quantum. Electron.* **1974**, *10*, 375−386.

(12) Cheng, J.; Chen, M.; Kafka, K.; Austin, D.; Wang, J.; Xiao, Y.; Chowdhury, E. Determination of ultra-short laser induced damage threshold of KH_2PO_4 crystal: Numerical calculation and experimental verification. *AIP Adv.* **2016**, *6*, No. 035221.

(13) Feit, M. D.; Rubenchik, A. M.; Faux, D. R.; Riddle, R. A.; Shapiro, A. B.; Eder, D. C.; Penetrante, B. M.; Milam, D.; Genin, F. Y.; Kozlowski, M. R. Modeling of laser damage initiated by surface contamination. In *Laser-Induced Damage in Optical Materials*; International Society for Optics and Photonics: 1997, *2966*, 417−424.

(14) Maunier, C.; Balas, M.; Donval, T.; Lamaignère, L.; Duchateau, G.; Mennerat, G. Self-laser conditioning of KDP and DKDP crystals. In *Laser-Induced Damage in Optical Materials*; International Society for Optics and Photonics: 2011, *8190*, 819018.

(15) Cheng, J.; Chen, M.; Liao, W.; Wang, H.; Wang, J.; Xiao, Y.; Li, M. Influence of surface cracks on laser-induced damage resistance of brittle KH_2PO_4 crystal. *Opt. Express* **2014**, *22*, 28740−28755.

(16) Chen, M.-J.; Cheng, J.; Li, M.-Q.; Xiao, Y. Study of modulation property to incident laser by surface micro-defects on KH_2PO_4 crystal. *Chin. Phys. B* **2012**, *21*, No. 064212.

(17) Chambonneau, M.; Lamaignère, L. Multi-wavelength growth of nanosecond laser-induced surface damage on fused silica gratings. *Sci. Rep.* **2018**, *8*, 891.

(18) De Yoreo, J. J.; Burnham, A. K.; Whitman, P. K. Developing KH_2PO_4 and KD_2PO_4 crystals for the world's most power laser. *Int. Mater. Rev.* **2013**, *47*, 113−152.

(19) Campbell, J. H.; Hawley-Fedder, R. A.; Stolz, C. J.; Menapace, J. A.; Borden, M. R.; Whitman, P. K.; Yu, J.; Runkel, M. J.; Riley, M. O.; Feit, M. D.; Hackel, R. P. NIF optical materials and fabrication technologies: an overview. In *Optical Engineering at the Lawrence Livermore National Laboratory II: The National Ignition Facility*; International Society for Optics and Photonics: 2004, *5341*, 84.

(20) Yang, H.; Cheng, J.; Chen, M.; Wang, J.; Liu, Z.; An, C.; Zheng, Y.; Hu, K.; Liu, Q. Optimization of morphological parameters for mitigation pits on rear KDP surface: experiments and numerical modeling. *Opt. Express* **2017**, *25*, 18332−18345.

(21) Guss, G.; Bass, I.; Draggoo, V.; Hackel, R.; Payne, S.; Lancaster, M.; Mak, P. Mitigation of growth of laser initiated surface damage in fused silica using a 4.6-micron wavelength laser. In *Laser-Induced Damage in Optical Materials*; International Society for Optics and Photonics: 2007, *6403*, 64030M.

(22) Feit, M. D.; Rubenchik, A. M. Influence of subsurface cracks on laser-induced surface damage. In *Laser-Induced Damage in Optical Materials*; International Society for Optics and Photonics: 2004, *5273*, 264.

(23) Carr, C. W.; Radousky, H. B.; Rubenchik, A. M.; Feit, M. D.; Demos, S. G. Localized dynamics during laser-induced damage in optical materials. *Phys. Rev. Lett.* **2004**, *92*, No. 087401.

(24) Demos, S. G.; Negres, R. A.; Raman, R. N.; Rubenchik, A. M.; Feit, M. D. Material response during nanosecond laser induced breakdown inside of the exit surface of fused silica. *Laser Photonics Rev.* **2013**, *7*, 444−452.

(25) Kar, A.; Rockstroh, T.; Mazumder, J. Two-dimensional model for laser-induced materials damage: Effects of assist gas and multiple reflections inside the cavity. *J. Appl. Phys.* **1992**, *71*, 2560−2569.

(26) Boling, N. L.; Dubé, G.; Crisp, M. D. Morphological asymmetry in laser damage of transparent dielectric surfaces. *Appl. Phys. Lett.* **1972**, *21*, 487−489.

(27) Duchateau, G.; Feit, M. D.; Demos, S. G. Strong nonlinear growth of energy coupling during laser irradiation of transparent dielectrics and its significance for laser induced damage. *J. Appl. Phys.* **2012**, *111*, No. 093106.

(28) Bercegol, H.; Bonneau, F.; Bouchut, P.; Combis, P.; Gallais, L.; Lamaignere, L.; Natoli, J.-Y.; Rullier, J.-L.; Vierne, J. Comparison of numerical simulations with experiment on generation of craters in silica by a laser. In *Laser-Induced Damage in Optical Materials: 2002 and 7th International Workshop on Laser Beam and Optics Characterization*; International Society for Optics and Photonics: 2003, *4932*, 297−308.
(29) Wong, J.; Ferriera, J. L.; Lindsey, E. F.; Haupt, D. L.; Hutcheon, I. D.; Kinney, J. H. Morphology and microstructure in fused silica induced by high fluence ultraviolet 3ω (355nm) laser pulses. *J. Non-Cryst. Solids* **2006**, *352*, 255−272.
(30) Garcia-Lechuga, M.; Puerto, D.; Fuentes-Edfuf, Y.; Solis, J.; Siegel, J. Ultrafast moving-spot microscopy: birth and growth of laserinduced periodic surface structures. *ACS Photonics* **2016**, *3*, 1961−1967.
(31) Carr, C. W.; Matthews, M. J.; Bude, J. D.; Spaeth, M. L. The effect of laser pulse duration on laser-induced damage in KDP and SiO_2. In *Laser-Induced Damage in Optical Materials*; International Society for Optics and Photonics: 2006, *6403*, 64030K.
(32) Agranat, M. B.; Chefonov, O. V.; Ovchinnikov, A. V.; Ashitkov, S. I.; Fortov, V. E.; Kondratenko, P. S. Damage in a Thin Metal Film by High-Power Terahertz Radiation. *Phys. Rev. Lett.* **2018**, *120*, No. 085704.
(33) Manenkov, A. A. Fundamental mechanisms of laser-induced damage in optical materials: today's state of understanding and problems. *Opt. Eng.* **2014**, *53*, No. 010901.
(34) Carr, C. W.; Bude, J. D.; DeMange, P. Laser-supported solid-state absorption fronts in silica. *Phys. Rev. B* **2010**, *82*, 184304.
(35) Duchateau, G.; Hébert, D.; Hallo, L. Modeling of laser-induced damage in KDP crystals by nanosecond pulses: a preliminary hydrodynamic study. In *Laser-Induced Damage in Optical Materials*; International Society for Optics and Photonics: 2010, *7842*, 78420S.
(36) Gamaly, E. G.; Rode, A. V.; Luther-Davies, B.; Tikhonchuk, V. T. Ablation of solids by femtosecond lasers: Ablation mechanism and ablation thresholds for metals and dielectrics. *Phys. Plasmas* **2002**, *9*, 949−957.
(37) Chandrasekhar, S. *Hydrodynamic and hydromagnetic stability*; at the Clarendon Press: 1961, 109−154.
(38) Courtois, M.; Carin, M.; Le Masson, P.; Gaied, S.; Balabane, M. A new approach to compute multi-reflections of laser beam in a keyhole for heat transfer and fluid flow modelling in laser welding. *J. Phys. D: Appl. Phys.* **2013**, *46*, 505305.
(39) Hébert, D.; Hallo, L.; Voisin, L.; Desanlis, T.; Galtié, A.; Bicrel, B.; Maunier, C.; Mercier, P.; Duchateau, G. A KDP equation of state for laser-induced damage applications. *J. Appl. Phys.* **2011**, *109*, 123527.
(40) Esmaeeli, A.; Tryggvason, G. Computations of film boiling. Part I: numerical method. *Int. J. Heat Mass Transfer* **2004**, *47*, 5451−5461.
(41) DeMange, P.; Negres, R. A.; Raman, R. N.; Colvin, J. D.; Demos, S. G. Role of phase instabilities in the early response of bulk fused silica during laser-induced breakdown. *Phys. Rev. B* **2011**, *84*, No. 054118.
(42) Guo, Z.; Lin, P. A thermodynamically consistent phase-field model for two-phase flows with thermocapillary effects. *J. Fluid Mech.* **2015**, *766*, 226−271.
(43) Liu, Q.; Cheng, J.; Xiao, Y.; Chen, M.; Yang, H.; Wang, J. Effect of tool inclination on surface quality of KDP crystal processed by micro ball-end milling. *Int. J. Adv. Manuf. Technol.* **2018**, 2777.
(44) Zhang, L.; Chen, W.; Hu, L. Systematic investigation on light intensification by typical subsurface cracks on optical glass surfaces. *Appl. Opt.* **2013**, *52*, 980−989.
(45) Fang, T.; Lambropoulos, J. C. Microhardness and indentation fracture of potassium dihydrogen phosphate (KDP). *J. Am. Ceram. Soc.* **2002**, *85*, 174−178.
(46) Raman, R. N.; Negres, R. A.; Demos, S. G. Time-resolved microscope system to image material response following localized laser energy deposition: exit surface damage in fused silica as a case example. *Opt. Eng.* **2011**, *50*, No. 013602.
(47) Fathi, A.; Chung, C.-Y.; Lee, Y.-P.; Diau, E. W.-G. Label-free optical microscope based on a phase-modulated femtosecond pump−probe approach with subdiffraction resolution. *ACS Photonics* **2020**, *7*, 607−613.

https://dx.doi.org/10.1021/acsomega.0c02950
ACS Omega 2020, 5, 19884−19895